Chapter 20

Multimodal Imaging of Cerebral Microhemorrhages and White Matter Degradation in Geriatric Patients with Mild Traumatic Brain Injury

Maria Calvillo, Di Fan, and Andrei Irimia

Abstract

Traditionally, neurobiologists have utilized *microscale* techniques of scientific investigation to uncover the fundamental organization and function of brain cells and neuronal ensembles. In recent decades, however, *macroscale* brain imaging methods like magnetic resonance imaging (MRI) and computed tomography (CT) have facilitated a wider scope of understanding neural structure and function across the lifespan. Thanks to such methods, a broader picture of the relationship between microscale processes—studied by neurobiologists—and macroscale observations—made by clinicians—has emerged. More recently, the vascular component of neurodegeneration has come under renewed scrutiny partly due to increased appreciation of the relationship between neurovascular injury, cardiovascular disease, and senescence. Cerebral microbleeds (CMBs) are among the smallest lesions of the cerebrum which can be visualized using MRI to indicate blood–brain barrier (BBB) impairment; as such, this class of hemorrhages are important for the evaluation and macroscale detection of geriatric patients' microscale pathologies associated with neurovascular disease and/or neurodegeneration. This chapter details a streamlined protocol for MRI/CT multimodal imaging data acquisition, archiving and digital processing, including methods tailored for the analysis of susceptibility-weighted imaging (SWI) and diffusion-weighted imaging (DWI) scans to reveal CMB-related alterations of the human connectome. Efficient and effective MRI/CT methods like ours, when tailored for CMB and connectome analysis, are essential for future progress in this important field of scientific inquiry.

Key words Magnetic resonance imaging, Computed tomography, Diffusion tensor imaging, Susceptibility-weighted imaging, Cerebral microbleed, Aging, Geriatrics, Image processing, Traumatic brain injury, Cognitive impairment

1 Introduction

Microscale alterations effected upon the brain by neurological and metabolic disease are typically studied by cell biologists at the level of cells and neuronal assemblies using *microscale* imaging techniques. Nevertheless, *macroscale* imaging methods like magnetic resonance imaging (MRI) and computed tomography (CT) may complement such efforts by enabling scientists to relate microscale

Sean P. Curran (ed.), *Aging: Methods and Protocols*, Methods in Molecular Biology, vol. 2144,
https://doi.org/10.1007/978-1-0716-0592-9_20,

pathology to macroscale findings, thereby offering a broader picture of aging and neurodegeneration. Throughout the past two decades, multisite brain imaging studies have become increasingly common, such that it is vital for imaging data to be acquired, processed and analyzed using streamlined workflows which minimize site-related differences in acquisition and analysis procedures. The adequate management of imaging data acquired from older adult populations has special significance, given geriatric patients' higher rates of overall morbidity, neurologic disease and neuropathology incidence. For example, persons aged 65 and older are more vulnerable to traumatic brain injury (TBI)—particularly mild TBI (mTBI)—and mild cognitive impairment (MCI) than any other group of adults; this can lead to substantially lower quality of life compared to younger individuals, often in tandem with cardiovascular, neurovascular, neurological, and metabolic diseases, including dementia [1].

Improving the validity and reliability of procedures for the analysis of brain imaging data acquired from vulnerable populations—like the elderly—is of high priority in geriatrics and gerontology research. To achieve such improvement, research procedures and protocols must be described in detail, recorded thoroughly and published. Openly available protocol descriptions can improve the reproducibility of neuroimaging studies, define reference workflows for the implementation of multisite studies, and clarify methodological imprecisions to both scientists and clinicians.

In recent years, the vascular component of neurodegeneration has received increased attention due to mounting evidence on the relationship between neurovascular injury, cardiovasculardisease and aging. Cerebral microbleeds (CMBs) are parenchymal lesions of the cerebrum which can indicate impairment of the blood–brain barrier (BBB). They may be small as ~1 mm^3 on certain types of MRI [1], and are diagnostically important in geriatric patients because they represent macroscale manifestations of microscale pathological processes associated with neurovascular disease and neurodegeneration. This chapter describes a set of standardized, streamlined methods for the acquisition, processing and comprehensive analysis of CMB-positive MRI/CT scans of the aging brain, including the specification of suitable inclusion and exclusion criteria for older participants, MRI and CT scanner specifications, MRI imaging sequence parameters, data archiving strategies and processing methods for both CT and MRI, including T_1- and T_2-weighted anatomic MRI, diffusion-weighted imaging (DWI), and susceptibility-weighted imaging (SWI, which can assist in identifying CMBs) [1].

2 Methods

The first part of this section outlines procedures to recruit volunteers for imaging studies like those previously undertaken by our laboratory. This is followed by a description of our data acquisition protocol and then by a detailed narrative of data archiving and processing steps to prepare data for subsequent CMB analysis and connectomics.

2.1 Inclusion and Exclusion Criteria

The following are inclusion and exclusion criteria for older healthy control (HC) participants, for individuals with MCI and for TBI survivors.

2.1.1 Inclusion Criteria for All Groups

1. Be at least 40 years of age.
2. Speak English fluently.
3. Be competent to provide informed consent.

2.1.2 Exclusion Criteria for All Groups

1. A diagnosis of comorbid neurological or psychiatric disease.
2. Being currently nursing or pregnant, or intending to become pregnant.
3. Not speaking English fluently.
4. Suffering from AIDS.
5. Suffering from claustrophobia.
6. Having any metal objects in the body which are affected by strong magnetic fields.

2.1.3 Additional, Group-Specific Inclusion Criteria

1. For TBI participants, the volunteer must have experienced one or more TBIs.
2. For MCI participants, the volunteer must have reported memory concerns.

2.2 Data Acquisition and Archiving

2.2.1 MRI Acquisition

MRIs are acquired using a whole-body, MAGNETOM Prisma^{FIT} 3T scanner (Siemens Corporation, Erlagen, Germany) with a 60 cm bore diameter. All head scans are acquired using a 20-channel head–neck matrix coil. The following are the technical specifications of the Prisma^{FIT} scanner:

1. Magnetic homogeneity of 0.103 parts per million (ppm) within the 40 cm diameter spherical volume of the bore.
2. 64 parallel radiofrequency (RF) receiver channels and up to 204 coil elements.
3. Dual-channel parallel transmit and slice-accelerated "multiband" acquisition.
4. A total imaging matrix (TIM) of 204 $\times$ 64.
5. A 2$\times$ Tesla C2075 graphics processing unit (GPU).

6. A XR 80/200 gradient system with a maximum amplitude of 80 mT/m per axis and a maximum slew rate of 200 T/m/s per axis.
7. Active shimming using three linear and five second-order channels.
8. A field of view (FOV) of at most 500 mm and at least 5 mm.
9. A maximum matrix size of 1024 × 1024.
10. A maximum in-plane resolution of 7 μm.
11. Integrated Tx/Rx solid-state DirectRF technology.
12. Syngo MR VD13D software.

A total of ten sequences are included in this protocol for acquiring MRI scans. The sequence names and their parameters are listed in Table 1.

Table 1
MRI acquisition parameters

Parameter	Unit	MPRAGE T1	FSE T1	T2	FLAIR	FLASH	fMRI	GRE SWI	DWI
Repetition time (TR)	ms	30	3.15	3.15	3.15	800	10,000	1950	8300
Echo time (TE)	ms	20	1.37	1.37	1.37	20	88	2.98	72
Inversion time (TI)	ms	–	–	–	–	–	–	900	–
Pixel width	mm	0.5	1.625	1.6	1.6	1	0.82	1	2
Pixel height	mm	0.5	1.625	1.6	1.6	1	0.82	1	2
Slice thickness	mm	2	1.6	1.6	1.6	4	3.5	1	2
Interslice gap	mm	0	0	0	0	5.2	3.5	0	2
Sampling	%	50	100	100	100	100	100	100	100
Phase FOV	%	75	100	100	100	75	100	100	100
Pixel bandwidth	Hz	100	540	540	540	180	200	240	1345
Flip angle	°	15	8	8	8	20	120	9	90
Echo train length (ETL)	–	1	1	1	1	1	17	1	47
Acquisition matrix width	–	384	160	162	162	192	256	256	128
Acquisition matrix height	–	512	160	162	162	256	256	256	128
Acquisition type	–	3D	3D	3D	3D	2D	2D	3D	2D
Number of averages	–	1	1	1	1	1	1	1	1
Echo number	–	1	1	1	1	1	1	1	1
Phase encoding steps	–	191	118	118	118	269	333	255	95
Phase encoding direction	–	ROW	ROW	ROW	ROW	ROW	ROW	ROW	COL

Listed here are selected parameters for eight MRI sequences, as utilized with the acquisition protocol described. Importantly, (A) the TR, TE and TI are fundamental temporal parameters which determine the properties of the MRI signal, whereas (B) pixel width, height, slice thickness, and interslice gap determine the spatial resolution of a scan

2.2.2 CT Acquisition

CT scans are acquired using a 16-slice General Electric (GE) BrightSpeed™ scanner. Images are acquired using the following parameters:

1. Width: 512 pixels.
2. Height: 512 pixels.
3. Mode: helical.
4. Slice thickness: 0.6250 mm.
5. Slice spacing: 0.6250 mm.
6. Kilovoltage peak (kVp): 120 kV.
7. Data collection diameter: 250 mm.
8. Reconstruction diameter: 223 mm.
9. Gantry detector tilt: 0°.
10. Rotation direction: clockwise.
11. Exposure time: 1397 ms.
12. X-ray tube current: 140 mA.
13. Filter type: head filter.
14. Generator power: 16,800 kW.
15. Focal spot: 0.7 mm.
16. Convolution kernel type: soft.
17. Revolution time: 1 s.
18. Single collimation width: 0.625 mm.
19. Total collimation width: 10 mm.
20. Table speed: 9.3750 mm/s.
21. Table feed per rotation: 9.375 mm.
22. Spiral pitch factor: 0.9375.
23. Pixel spacing: 0.435547 mm.

2.2.3 MRI/CT Archiving

After acquisition, data are stored in DICOM (digital imaging and communications in medicine) format. They are then deidentified and delinked to preserve privacy and confidentiality. This is achieved by removing identifying information from the DICOM file headers. Next, data are transferred to a secure online database managed by the scanning facility (*see* **Note 1**). Following this transfer, data are transferred to a depository maintained by the laboratory, where they can be accessed and processed at ease (*see* **Note 2**).

2.3 Neuroimage Data Processing

All data processing steps are based upon protocols used in past studies conducted in our laboratory [2–7]. This section describes preprocessing steps for both MRI and CT scans. A set of universal MRI processing steps are applied to all MRI volumes, whereas DWI

and SWI data undergo additional processing steps which are specific only to these two types of data. All steps for universal MRI processing and DTI are undertaken using the fMRI Standard Library (FSL) image processing toolbox (fsl.fmrib.ox.ac.uk/fsl).

2.3.1 MRI Preprocessing Steps

The following set of preprocessing steps is applied to all MRI volumes, including those acquired using DWI and SWI sequences.

1. DICOM files are converted into NIFTI format using dcm2niix (https://www.nitrc.org/plugins/mwiki/index.php/dcm2nii:MainPage).
2. Motion correction is performed.
3. Voxels beyond the area of the brain are excluded (i.e., imaging volumes are skull-stripped).
4. Image intensities within the brain mask are identified.
5. The intensities of voxels within the brain are normalized across subjects by dividing their intensities by their median intensity (*see* **Note 3**).
6. Bias field correction is applied to each volume using a fourth-order polynomial [8].

2.3.2 DWI Processing Steps

The following steps are applied to DWI data in addition to those previously described.

1. B_0 volumes are identified as those volumes acquired while no diffusion gradient is being applied.
2. Skull removal is implemented and the brain mask is computed.
3. Susceptibility artifact correction is implemented.
4. Motion correction is applied.
5. Eddy-current artifact correction is performed.
6. A suitable rotation of the B matrix is applied to alleviate orientation artifacts (*see* **Note 4**).
7. B_0 images are coregistered to their corresponding T_1-weighted volumes using a rigid, affine (six-parameter) registration.
8. Diffusion tensors are fitted to DWI images.
9. Fractional anisotropy (FA) calculations are performed.
10. Deterministic tractography via fixed step-length streamline propagation is used to reconstruct white matter (WM) streamlines using the following parameters:
    - Seed spacing: 0.5 mm.
    - Linear measure start threshold: 0.3.
    - Stopping value: 0.17.
    - Minimum streamline length: 20 mm.

- Maximum streamline length: 110 mm.
- Stopping criterion: fa value.
- Stopping criterion value: 0.17.
- Stopping track curvature: 0.96 mm^{-1}.
- Integration step length: 0.5 mm.

11. Streamlines are visualized in TrackVis (trackvis.org) and 3D Slicer (www.slicer.org).

If longitudinal MRI/DWI data are available, one can estimate and reduce the extent to which diffusion tractography measures can be influenced by confounding factors, such as subject motion, scanner noise, MRI inhomogeneity differences and other computational errors and inaccuracies. Such estimation is completed through the following technique:

1. At each WM voxel, the uncertainty ellipsoid is defined as a volume around a voxel where any DTI-derived WM measures require detailed analysis, since they may be influenced by confounding factors to a greater extent (*see* **Note 5**).
2. If quantification of WM changes over time is required, the following steps are taken:
   (a) Streamlines are assumed to be piecewise-differentiable 3D space curves with an invariant curvature and torsion.
   (b) Any two curves are determined to have equal curvature and torsion if they lie within the same transformation of each other and if there is a curve index correspondence between parametrizations.
   (c) Within each subject, curve index correspondence is established [9] by generating arc length parametrizations for each curve, time point, and perilesional streamline bundle.
   (d) Point-to-point coregistration is performed by implementing a local transformation using Schönemann's solution to the orthogonal Procrustes problem [10].
   (e) The global residue of squared intercurve distances within the local transformations is minimized to approximate a global transformation which matches source and target curves.
   (f) FA values and pointwise descriptive statistics of each measure are calculated for the arc-length coordinates of each streamline [9, 11].
   (g) The range of arc-length coordinates shared between most streamlines within each bundle of interest is identified.

(h) To compare mean FA differences over time within perilesional streamline bundles and then evaluate whether or not they may be due to artifacts, two empirical reference mean FA distributions are established (one for younger subjects and one for older subjects).

(i) The mean and variance of the reference distributions are calculated over the streamlines.

(j) Distribution parameter values are pooled within each age group.

(k) The null hypothesis of no difference in FA across time points is tested for each perilesional streamline bundle of interest.

3. WM streamline prototyping is implemented as follows:

(a) An anatomical clustering atlas is used to annotate and categorize WM streamline clusters (*see* **Note 6**) as deep WM bundles (such as major association and projection bundles, commissural bundles, cerebellar and brainstem connection bundles), short bundles and medium-range superficial bundles, which are organized by the brain lobes that they connect.

(b) Connections identified as potential false positives are annotated for exclusion.

(c) Following WM parcellation, WM prototyping is implementing by identifying the most representative WM streamline in each cluster, that is, the streamline whose trajectory is most similar to the average trajectory of the streamline in the bundle (*see* **Note 7**).

2.3.3 SWI Processing Steps

The following steps are implemented to process SWI volumes and identify CMBs:

1. SWI volumes are skull-stripped and coregistered rigidly to their respective T_1-weighted volumes.
2. CMB identification is accomplished using the following algorithms.
   - The image intensity gradient of the skull-stripped SWI volume is computed at each brain voxel using MATLAB.
   - Binary erosion of the gradient magnitude volume is performed using a spherical morphological structuring element (radius = 11 pixels) to remove areas exhibiting sharp gradient changes at the edges of the brain.
   - A gradient magnitude histogram is calculated over all brain voxels.

- The eroded volume is thresholded to exclude values belonging to the tails of its intensity distribution.
- Within the thresholded volume, the volume of each connected component consisting of contiguous nonzero voxels is computed.
- The largest component—associated with voxels on the borders between cerebrospinal fluid (CSF) and WM—is removed.
- Components associated with voxels within the sulcal banks of the neocortex and on the boundaries between brain and blood vessels are eliminated by removing voxels which were identified as isointense (i.e., within $\mu \pm 2\sigma$ of the image intensity distribution of the SWI image).
- Remaining nonzero voxel components are assigned CMB labels.

The sensitivity and precision of the CMB identification method can be evaluated against a manual CMB labeling method conducted by a neuroanatomy and neuroradiology expert. Specifically, to calculate the sensitivity and precision of the approach, a manual detection algorithm is used, as follows.

1. Potential CMBs are identified in images using a voxel classifier based on Microbleed Anatomic Rating Scale (MARS) guidelines [12].
2. Identified CMBs are classified as either certain (represented by small, clearly delineated circular shapes) or doubtful (represented as components which are not well-delineated and which do not conform to strictly circular shapes).
3. Hypointensities on the boundary of the brain are disregarded, as CMBs are not associated with the meninges.
4. An object-based classifier which assesses CMB shape is applied to eliminate false positives CMB assignments.
5. CMB sphericity violations are determined by calculating CMB object curvature and identifying values which exceed the curvature of a sphere by a substantial amount [13].
6. If CMB etiology must be classified as either traumatic or nontraumatic (e.g., related to cerebral amyloid angiopathy or hypertensive vasculopathy), a CMB is assumed to be TBI-related if (A) at the acute stage of TBI, the CMB is partially or fully surrounded by one or more focal FLAIR hyperintensities, and (B) at the chronic stage of TBI, the FLAIR hyperintensities are no longer detectable.

2.3.4 CT Processing Steps

CT segmentation is performed using an approach whose results are presented elsewhere [14–19]. The steps of the algorithm are as follows.

1. The parameters of Gaussian intensity distributions are computed for three tissue classes [WM, gray matter (GM), and cerebrospinal fluid (CSF)].
2. Using the following steps, probabilities are assigned to voxels to reflect their likelihood of belonging to a specific tissue class in the Gaussian mixture model:
   (a) An objective function is derived from several Gaussian random variable models and its value is minimized using a nonlinear optimization procedure of the user's choice.
   (b) To complete the classification process, a priori tissue probability maps available in a modified MINI_{152} probabilistic atlas [20] are identified for each tissue class.
   (c) To accommodate the intensity profile of CT scans—where CSF is hypointense—the atlas is modified to assign low intensities to CSF voxels in the atlas.
   (d) The objective function is used to weigh the probability maps using Bayesian inference principles.
   (e) The probability maps are deformed to match each subject's brain CT volumes to be segmented.
   (f) The volumes are segmented by assigning probabilities to each voxels, which specify the likelihood that the voxel belongs to a certain tissue class.
   (g) Posterior probabilities are computed according to each subject's voxel intensity values.
   (h) The interface between the resulting GM and WM volumes is smoothed using a nonlinear Wiener filter, subject to the topological constraints of the brain's intensity profile.
   (i) Topology-constrained probabilistic classification refinement is performed [16] in three steps:
      - The plane which crosses the WM/GM boundary and is intersected by voxels with minimal intensity variance is identified.
      - Voxels in the identified plane are assigned according to whether most of them have an unclear intensity classification, or whether they are close to voxels with varying class memberships.
      - A voxel's class assignment is changed to the more appropriate one if this reduces the in-plane density variance.

Figure 1 shows the output produced by the preprocessing of DWI and SWI scans acquired from a sample geriatric mTBI patient.

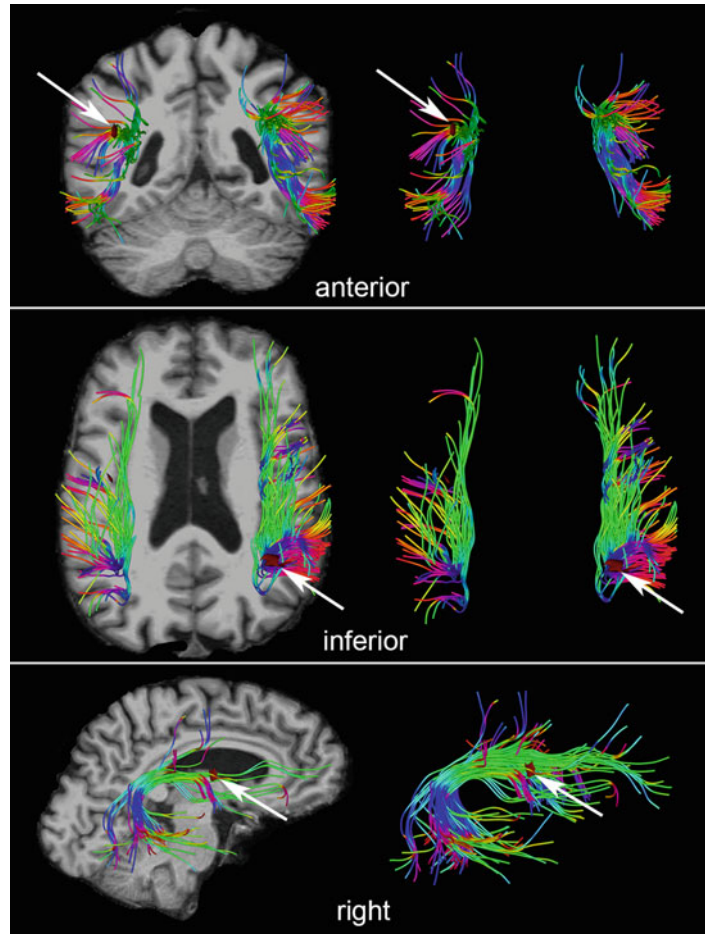

Fig. 1 Example output of a DWI/SWI analysis revealing the colocalization of two CMBs (arrows) relative to the arcuate fasciculus (AF) of the two cerebral hemispheres. The AF is a WM structure with substantial involvement in speech production. Two CMBs are depicted as small, red, ovoidal objects located in the spatial vicinity of the AF. Shown are anterior (top row), inferior (middle row), and right (bottom row) views of the cerebral cortex, cerebellum, lateral ventricles and brain stem. Because of their locations, only one CMB is visible in any of the three views. Specifically, one (smaller) CMB is visible in the anterior and lateral views (top and bottom rows), and one (larger) CMB is visible in the inferior view (middle row). T_1-weighted images of the cortex are overlaid to indicate the location of the CMBs and AF relative to the anatomy of the brain. WM streamline orientation is color-coded (red: left to right; green: anterior to posterior; blue: inferior to superior). The left column localizes the AF relative to the brain, whereas the right column isolates this WM structure for easier visualization

3 Notes

1. Interaction with the secure database to which the MRI scans were uploaded is facilitated by Flywheel software (flywheel.io).
2. MRI data transfer is made to a HIPAA-compliant Amazon Web Services (AWS) online cloud environment.
3. Intensity normalization is implemented to account for the potentially confounding effect of inter-subject intensity brain differences.
4. The additional rotation of the B matrix in DWI image processing is necessary because resulting orientational information may be affected by the increased head motion which is often associated with DWI, given this modality's relatively long acquisition times [21].
5. In the estimation of confounding factors, the use of the ellipsoid—rather than that of a sphere—is advantageous because it facilitates the evaluation of the local water-diffusion WM anisotropy.
6. The anatomically curated streamline clustering atlas used is described in reference [6]. This atlas is suitable because it allows the whole-brain WM to be parceled into 800 streamline clusters.
7. The approach to WM prototyping was based upon methods described elsewhere [3, 6, 7, 9, 22]. Streamline prototyping is important in diffusion MRI tractography, as the latter technique may generate false streamlines which are not representative of real WM connections. Establishing a streamline prototype for an entire cluster allows for a more accurate detection of underlying WM structure and of its trajectory.

Acknowledgments

This work was supported by NIH grant R01 NS 100973, by DoD contract W81-XWH-1810413 and by the Undergraduate Research Associate Program (URAP) at the University of Southern California. The authors wish to thank Nikhil N. Chaudhari, Nahian F. Chowdhury, and Kenneth A. Rostowsky for their comments and suggestions, as well as Drs. Lauren J. O'Donnell and Fan Zhang (Harvard Medical School) for their advice on DWI preprocessing. AI would like to thank the Department of Electrical Engineering and Computer Science at the Massachusetts Institute of Technology, where part of this research was carried out.

References

1. Irimia A, Van Horn JD, Vespa PM (2018) Cerebral microhemorrhages due to traumatic brain injury and their effects on the aging human brain. Neurobiol Aging 66:158–164. https://doi.org/10.1016/j.neurobiolaging.2018.02.026
2. Fan D, Chaudhari NN, Rostowsky KA, Calvillo M, Lee SK, Chowdhury NF, Zhang F, O'Donnell LJ, Irimia A (2019) Post-traumatic cerebral microhemorrhages and their effects upon white matter connectivity in the aging human brain. Conf Proc IEEE Eng Med Biol Soc 2019:198–203
3. Rostowsky KA, Maher AS, Irimia A (2018) Macroscale white matter alterations due to traumatic cerebral microhemorrhages are revealed by diffusion tensor imaging. Front Neurol 9:948. https://doi.org/10.3389/fneur.2018.00948
4. Irimia A, Maher AS, Rostowsky KA, Chowdhury NF, Hwang DH, Law EM (2019) Brain segmentation from computed tomography of healthy aging and geriatric concussion at variable spatial resolutions. Front Neuroinform 13:9–9. https://doi.org/10.3389/fninf.2019.00009
5. Maher AS, Rostowsky KA, Chouwdhury NF, Irimia A (2018) Neuroinformatics and analysis of connectomic alterations due to cerebral microhemorrhages in geriatric mild neurotrauma: microhemorrhages in geriatric neurotrauma. Paper presented at the Proceedings of the 2018 ACM international conference on bioinformatics, computational biology, and health informatics, Washington, DC, USA
6. Zhang F, Wu Y, Norton I, Rigolo L, Rathi Y, Makris N, O'Donnell LJ (2018) An anatomically curated fiber clustering white matter atlas for consistent white matter tract parcellation across the lifespan. Neuroimage 179:429–447. https://doi.org/10.1016/j.neuroimage.2018.06.027
7. Norton I, Essayed WI, Zhang F, Pujol S, Yarmarkovich A, Golby AJ, Kindlmann G, Wassermann D, Estepar RSJ, Rathi Y, Pieper S, Kikinis R, Johnson HJ, Westin C-F, O'Donnell LJ (2017) SlicerDMRI: open source diffusion MRI software for brain cancer research. Cancer Res 77(21):e101–e103. https://doi.org/10.1158/0008-5472.CAN-17-0332%J
8. Sled JG, Zijdenbos AP, Evans AC (1998) A nonparametric method for automatic correction of intensity nonuniformity in MRI data. IEEE Trans Med Imaging 17(1):87–97. https://doi.org/10.1109/42.668698
9. Donnell LJO, Westin C (2007) Automatic tractography segmentation using a high-dimensional white matter atlas. IEEE Trans Med Imaging 26(11):1562–1575. https://doi.org/10.1109/TMI.2007.906785
10. Leemans A, Sijbers J, De Backer S, Vandervliet E, Parizel P (2006) Multiscale white matter fiber tract coregistration: a new feature-based approach to align diffusion tensor data. Magn Reson Med 55(6):1414–1423. https://doi.org/10.1002/mrm.20898
11. Maddah M, Grimson WEL, Warfield SK, Wells WM (2008) A unified framework for clustering and quantitative analysis of white matter fiber tracts. Med Image Anal 12(2):191–202. https://doi.org/10.1016/j.media.2007.10.003
12. Gregoire SM, Chaudhary UJ, Brown MM, Yousry TA, Kallis C, Jäger HR, Werring DJ (2009) The Microbleed Anatomical Rating Scale (MARS). Reliability of a tool to map brain microbleeds. Neurology 73(21):1759–1766. https://doi.org/10.1212/WNL.0b013e3181c34a7d
13. Romeny BMT (2011) Multi-scale and multi-orientation medical image analysis. In: Deserno T (ed) Biomedical image processing. Springer Berlin, Heidelberg, pp 177–196. https://doi.org/10.1007/978-3-642-15816-2_7
14. Ashburner J, Friston K (1997) Multimodal image coregistration and partitioning—a unified framework. Neuroimage 6(3):209–217. https://doi.org/10.1006/nimg.1997.0290
15. Ashburner J, Friston KJ (2000) Voxel-based morphometry—the methods. Neuroimage 11(6):805–821. https://doi.org/10.1006/nimg.2000.0582
16. Ashburner J, Friston KJ (2005) Unified segmentation. Neuroimage 26(3):839–851. https://doi.org/10.1016/j.neuroimage.2005.02.018
17. Ashburner J, Friston K (2007) Segmentation. In: Friston K, Ashburner J, Kiebel S, Nichols T, Penny W (eds) Statistical parametric mapping. Academic Press, London, pp 81–91. https://doi.org/10.1016/B978-012372560-8/50006-1
18. Dale AM, Fischl B, Sereno MI (1999) Cortical surface-based analysis: I. Segmentation and surface reconstruction. Neuroimage 9(2):179–194. https://doi.org/10.1006/nimg.1998.0395
19. Fischl B, Sereno MI, Dale AM (1999) Cortical surface-based analysis: II. Inflation, flattening, and a surface-based coordinate system.

Neuroimage 9(2):195–207. https://doi.org/10.1006/nimg.1998.0396

20. Grabner G, Janke AL, Budge MM, Smith D, Pruessner J, Collins DL (2006) Symmetric atlasing and model based segmentation: an application to the hippocampus in older adults. In: Larsen R, Nielsen M, Sporring J (eds) Medical image computing and computer-assisted intervention – MICCAI 2006. Springer Berlin Heidelberg, Berlin, Heidelberg, pp 58–66
21. Leemans A, Jones DK (2009) The B-matrix must be rotated when correcting for subject motion in DTI data. Magn Reson Med 61 (6):1336–1349. https://doi.org/10.1002/mrm.21890
22. O'Donnell LJ, Westin C-F, Golby AJ (2009) Tract-based morphometry for white matter group analysis. Neuroimage 45(3):832–844. https://doi.org/10.1016/j.neuroimage.2008.12.023